

Transient analysis of electro-osmotic transport by a reduced-order modelling approach

R. Qiao¹ and N. R. Aluru^{2,*†}

¹*Department of Mechanical and Industrial Engineering, University of Illinois at Urbana-Champaign, Urbana, IL 61801, U.S.A.*

²*Department of General Engineering and Beckman Institute for Advanced Science and Technology, University of Illinois at Urbana-Champaign, Urbana, IL 61801, U.S.A.*

SUMMARY

Transient behaviour of electro-osmotic transport in typical electrokinetic channels is studied in this paper. The time needed for the electro-osmotic flow to reach steady-state exhibits multiple time scales depending on whether the flow is governed by either a viscous force, electrokinetic force or by a combination of both. When an intersection is present in the electrokinetic channel, such as in a cross or a T-channel, the flow in the main channel and in the intersection gets to steady-state at different times.

A weighted Karhunen–Loève (KL) decomposition method is proposed in this paper to generate the global basis function for reduced-order simulation. The key idea in a weighted KL approach is that, instead of minimizing a least-squares measure of ‘error’ between the linear subspace spanned by the basis functions and the observation space, we minimize the weighted ‘error’ between the two spaces. The global basis functions in a weighted KL approach can be generated by computing the singular value decomposition (SVD) of the matrix containing the weighted snapshots. We show that the weighted KL decomposition based reduced-order model is computationally more efficient and can capture the multiple time scales encountered in electro-osmotic transport much more effectively compared to the classical KL decomposition based reduced-order model. Copyright © 2003 John Wiley & Sons, Ltd.

KEY WORDS: transient electro-osmotic flow; reduced-order model; weighted Karhunen–Loève decomposition; singular value decomposition; microfluidics

1. INTRODUCTION

Currently, there is great interest in the development of micro total analysis systems (μ -TAS) which integrate sample handling, analysis, detection, signal processing as well as many other processes [1, 2]. A popular mechanism for transporting fluids in μ -TAS is electro-osmosis

*Correspondence to: N. R. Aluru, 3265 Beckman Institute, University of Illinois, 405 N. Mathews MC-251, Urbana, IL 61801, U.S.A.

†E-mail: aluru@uiuc.edu

Contract/grant sponsor: DARPA; contract/grant number: F30602-98-2-0718

Received 12 December 2001

Revised 27 March 2002

Accepted 26 April 2002

(also referred to as electro-osmotic flow). Electro-osmotic flow can be induced by applying an electric field to a fluid enclosed between capillary surfaces. Electro-osmotic flow plays an important role in capillary electrophoresis. For example, electro-osmosis directly influences the efficiency, resolution and reproducibility of sample separation. Steady-state analysis of electro-osmotic transport has been reported before [3–5]. The time needed for the fluid to reach steady-state can play a critical role in sample injection and separation. The time scales encountered in electro-osmosis can be understood by performing a transient analysis of electro-osmotic flow.

In this paper, we present the transient analysis of electro-osmotic transport in several typical electrokinetic geometries. The time needed for the flow to reach steady-state involves multiple time-scales, i.e. flow at different positions in the channel reaches steady-state at different times. Specifically, the flow near the wall reaches steady-state much more quickly compared to the flow in the centre of the channel. For flow along the centre line of the channel, the time to reach steady-state is directly proportional to the square of the width of the channel and inversely proportional to the viscosity of the fluid. Results also indicate that for cross- and T-junctions, under balanced applied potentials, the flow within the intersection can reach steady-state much more quickly compared to the flow in the centre of the main channel.

Classical approaches, such as explicit or implicit time-stepping schemes [6], can be employed for analysis of time-dependent problems. However, these techniques can be very expensive for complicated problems encountered in MEMS and Bio-MEMS. There is currently a growing interest in developing reduced-order modelling techniques for MEMS and Bio-MEMS. The motivation behind a reduced-order model is that if the system's behaviour is known *a priori* either from experimental or simulation data, then one can extract certain modes (also called basis functions) from the data and then reformulate the problem in terms of these modes to significantly reduce the complexity of the original problem. Since a system's dynamic behaviour is usually dominated by only a few modes, the total number of degrees of freedom can be reduced significantly in a reduced-order model (ROM) simulation [7]. By approximating the unknown solution in terms of the few modes that are known to be dominant, the ROM simulation is able to drastically reduce the computation cost without significantly compromising on the accuracy of the solution.

The development of reduced-order models involves two important steps—The first is the generation of global basis functions and the second is the solution of the governing equations using the global basis functions. Typically, a Galerkin procedure is used to solve the governing equations using the global basis functions [8–11]. A number of approaches can be used to generate global basis functions. For example, the basis functions can be obtained from the solution of a certain eigen-problem [8] or by Fourier decompositions [12]. However, many existing approaches work well only for simple geometries or they require a large number of basis functions to capture the system behaviour. A popular approach to generate global basis functions is to use a Karhunen–Loève (KL) decomposition [13]. Given a set of snapshots of solution (or data), KL decomposition generates global basis functions by minimizing a least-squares measure of ‘error’ between the linear subspace spanned by the basis functions and the snapshots. A singular value decomposition, that is mathematically equivalent to the Karhunen–Loève decomposition, of the matrix containing the snapshots generates a set of ‘optimal’ global basis functions of which the dominant few modes can be used as the low order or reduced-order model [7].

Many dynamical systems of interest exhibit both rapidly varying transients (where the solution changes rapidly over a small time scale) and slowly varying transients (where the solution changes slowly over a large time scale). If the rapidly varying transient is represented by very few snapshots, then the basis functions computed by the classical KL decomposition technique may not be effective in capturing the system dynamics. In this paper, we propose a weighted KL decomposition technique to generate the global basis functions. The basic idea is to assign a weight to each snapshot so that rapid transients in system dynamics can be captured much more effectively. The new global basis functions are computed by a singular value decomposition of the weighted snapshot matrix. Our results indicate that the weighted KL decomposition is more efficient compared to the standard KL decomposition technique. Specifically,

1. When the number of snapshots and global basis functions are fixed, typically, we get better accuracy with the weighted KL decomposition based reduced-order model technique.
2. When the number of snapshots is fixed, typically, we need less number of basis functions with a weighted KL technique to match the accuracy obtained with a standard KL technique.
3. When the number of basis functions is fixed, typically, we need less number of snapshots with a weighted KL technique to match the accuracy obtained by a standard KL technique.
4. Because of the above reasons, the reduced-order model based on a weighted KL technique is computationally more efficient compared to the reduced-order model based on a standard KL technique.

The rest of the paper is outlined as follows: In Section 2, we introduce the electro-osmotic transport model, in Section 3, we show results on transient electro-osmotic flow in several electrokinetic geometries, in Section 4, we introduce the weighted KL decomposition based reduced-order model, in Section 5, we show results on the reduced-order modelling and finally conclusions are presented in Section 6.

2. ELECTRO-OSMOTIC TRANSPORT MODEL

Fluid flow due to electrical potentials, also referred as electro-osmotic transport, is described by the Laplace equation, the Poisson–Boltzmann equation and the incompressible Navier–Stokes equations. A detailed description of the electro-osmotic transport model can be found in Reference [5]. The model includes:

$$\nabla^2 \phi = 0 \quad (1)$$

$$\nabla^2 \psi = \frac{1}{\lambda_D^2} \frac{RT}{F} \sinh \left(\frac{F\psi}{RT} \right) \quad (2)$$

$$\nabla \cdot \mathbf{u} = 0 \quad (3)$$

$$\frac{\partial \mathbf{u}}{\partial t} + (\mathbf{u} \cdot \nabla) \mathbf{u} = \nu \nabla^2 \mathbf{u} - \frac{1}{\rho} \nabla p + \frac{1}{\rho} \mathbf{F} \quad (4)$$

$$\mathbf{F} = 2Fc_0 \sinh\left(\frac{F\psi}{RT}\right) (\nabla\phi) \quad (5)$$

The Laplace equation (1) describes the potential in the device (or in the electrokinetic geometry) because of applied potentials and the Poisson–Boltzmann equation (2) describes the potential (ψ) in the device because of the ζ -potential at the solution–capillary interface. It should be noted that the electric potential caused by the applied voltage and the ζ -potential on the wall is assumed to be decoupled. This is valid when the Debye length is small compared to the channel width and the charge at the wall is not large [3]. These assumptions typically hold for microfluidic flows. Equations (3) and (4) describe the fluid flow in the device because of the applied and ζ -potential. Specifically, Equation (3) is the incompressible continuity equation and Equation (4) is the Navier–Stokes equation. In Equation (4), \mathbf{F} is the body force, the definition of which is given in Equation (5). The mathematical model stated in Equations (1)–(5) along with the appropriate initial and boundary conditions describes the transient electro-osmotic problem.

In an earlier paper [5], we presented a meshless finite cloud method to solve the electro-osmotic transport model. In particular, we have presented a semi-implicit multi-step (SIMS) technique for solution of the Navier–Stokes equations. In this paper, we employ the finite cloud method to solve the Laplace and the Poisson–Boltzmann equations and the SIMS technique combined with the finite cloud method for solution of the transient Navier–Stokes equations. Details on the various numerical techniques employed here can be found in Reference [5].

3. TRANSIENT ANALYSIS OF ELECTRO-OSMOTIC FLOW

3.1. Straight channel

The first test problem considered is the straight channel shown in Figure 1. Initially, the fluid is at rest and at $t = 0$ s, we apply a potential at reservoir 1 and hold reservoir 2 at ground. We also assume a uniform ζ -potential of $\zeta = -1$ mV on the wall. We have prescribed no-slip velocity conditions on the top and bottom walls, as well as $p = 0$ at the two reservoirs. We assume a Debye length of $2 \mu\text{m}$ (this will be justified later), and the fluid properties are identical to those used in Reference [5].

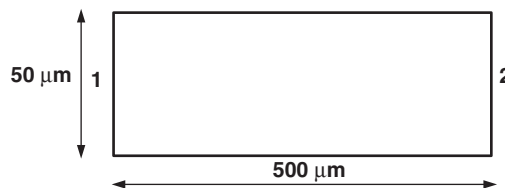


Figure 1. Geometry of a straight channel used for transient analysis.

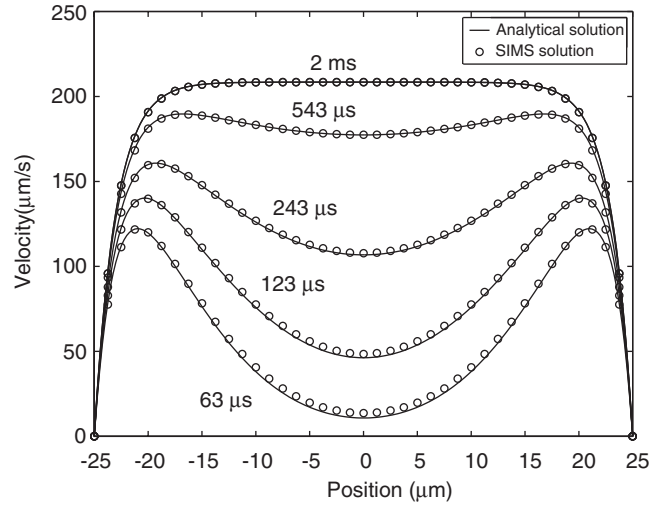


Figure 2. Comparison of computed and analytical solution for a straight channel. The ζ potential distribution is given by Equation (88) in Reference [5].

If we assume that the flow is fully developed in the channel, the above 2D problem reduces to a 1D problem. If the ζ -potential distribution is known, there exists an analytical solution for the x -component of the velocity given by Soderman and Jonsson [14]

$$\begin{aligned}
 u(y,t) = & \frac{\varepsilon E_x}{\mu} \{ \psi(y) - \psi(\pm L) + [\psi(\pm L) - \psi(0)] \\
 & \times \sum_{n=0}^{\infty} \frac{2(-1)^n}{(n + \frac{1}{2})\pi} \cos \left[\left(n + \frac{1}{2} \right) \pi \frac{y}{L} \right] \times \exp \left(- \frac{(n + \frac{1}{2})^2 \pi^2 \nu}{L^2} t \right) \} \quad (6)
 \end{aligned}$$

where ε is the permittivity of the solution, μ and ν are the dynamic and kinematic viscosity of the solution respectively, E_x is the electric field intensity in the x -direction, $\psi(y)$ is the solution to the Poisson–Boltzmann equation (Equation (2)), $\psi(\pm L)$ corresponds to the ζ -potential on the top and bottom walls, and $\psi(0)$ is the potential in the middle of the channel, typically zero. For $\zeta = -1$ mV, and $\phi_1 = 150$ V, the computed and analytical solution are shown in Figure 2.

The time for the fluid to reach steady-state (denoted by T_s) can be an important parameter in many applications [15]. Figure 3 shows that T_s for different positions in the channel differs greatly. The fluid close to or within the Debye layer reaches steady-state much more quickly compared to the fluid far away from the Debye layer. This is because the flow within the Debye layer is driven by electro-kinetic force while the flow in the central portion of the channel is driven by viscous forces. The electro-kinetic force acts on the fluid instantaneously when the external potentials are applied, while the viscous force acts on the fluid in the central part of the channel after a certain time. Also shown in Figure 3 is T_s for different positions in the channel if the flow is purely pressure-driven. It is clear that for a pressure driven flow,

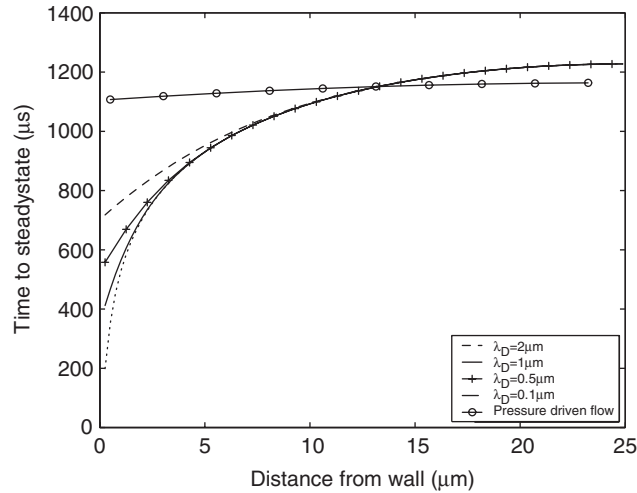


Figure 3. Velocity evolution at different positions in the channel.

the difference in T_s for different locations is much smaller compared to electro-osmotic flow. Calculation shows that the variation of T_s with channel width at the centre line of the channel follows the relationship:

$$T_s = 0.491h^2/\nu \quad (7)$$

where h is the channel width and ν is the fluid kinematic viscosity. This result is in accordance with the analytical result in Reference [3] though our coefficient is about 5% higher than that used in Reference [3]. The reason might be that only the first term of the infinite series was taken in the analysis of Reference [3], while such truncation error is not present in the current approach.

In the above simulation, the Debye length used is much higher than its actual value (typically, the Debye length is a few nanometers). This issue has been investigated before [3, 4], and the choice of artificial Debye length was explained and justified earlier in Reference [5] for steady-state calculations. An important concern is whether such a choice of artificial Debye length can still give a reliable estimate of important transient characteristics such as the time needed for the flow to reach steady-state. Figure 3 shows that when the Debye length is changed from 2.0 to 0.1 μm , T_s remains the same for the fluid in the centre of channel, but T_s near the wall (within 5 μm from the wall) changes significantly. However, if, for example, we choose a Debye length of 1 μm , then T_s will be accurate for a position of about 3.0 μm away from the wall. In practice, choice of a suitable Debye length is usually a compromise between accuracy of flow characteristics (flow rate, T_s and so on) and computational cost.

3.2. Cross channel

Figure 4 shows the cross channel geometry used in the simulations. The width of both horizontal (main channel) and vertical channels (side channel) is 30 μm . Figure 5 shows the evolution of velocity profile at a position far downstream of the main channel. This result is obtained by taking $\lambda_D = 1.5 \mu\text{m}$, prescribing a constant $\zeta = -1 \text{ mV}$ on all walls, grounding

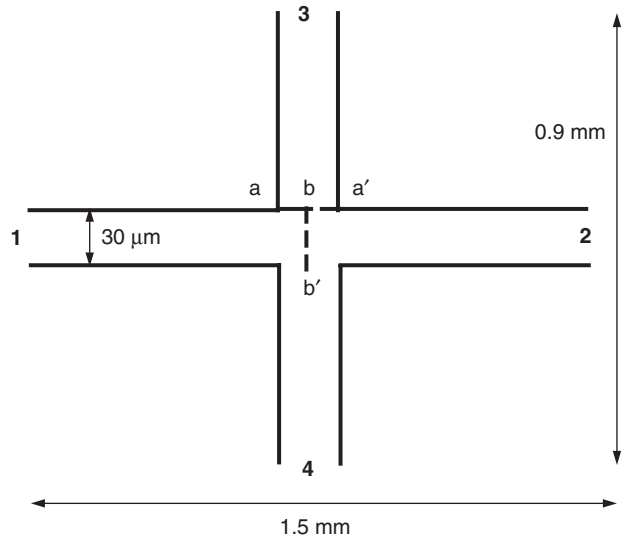


Figure 4. Geometry of a cross channel used in transient analysis.

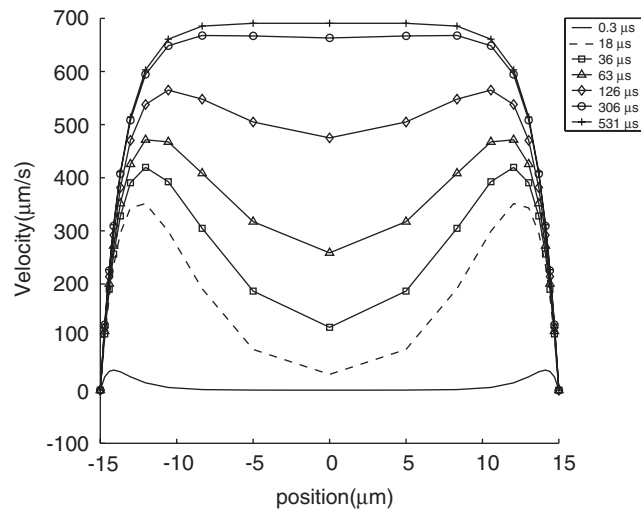


Figure 5. U-velocity (x-component of velocity) far downstream of the intersection.

reservoir 2, applying 1500V at reservoir 1, and applying 750V at reservoirs 3 and 4. Initially, the fluid is stationary and at $t=0$ s, applied potential is activated and the electro-kinetic force is used to drive the fluid. Simulations also show that the time needed to reach steady-state, at a position far away from the intersection is not influenced by the presence of the intersection. This is because the time needed to reach steady-state is dominated by either the electro-kinetic force (within the Debye layer) or the viscous force (in the central part of the channel), and

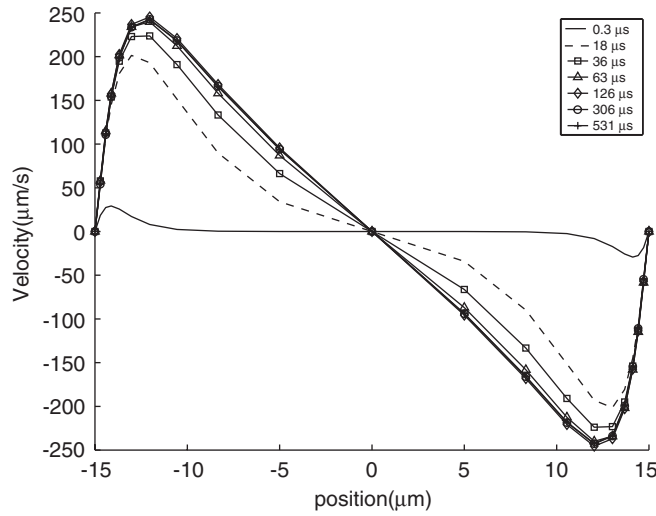


Figure 6. Evolution of V-velocity (y -component of velocity) at position $a - a'$ of Figure 4.

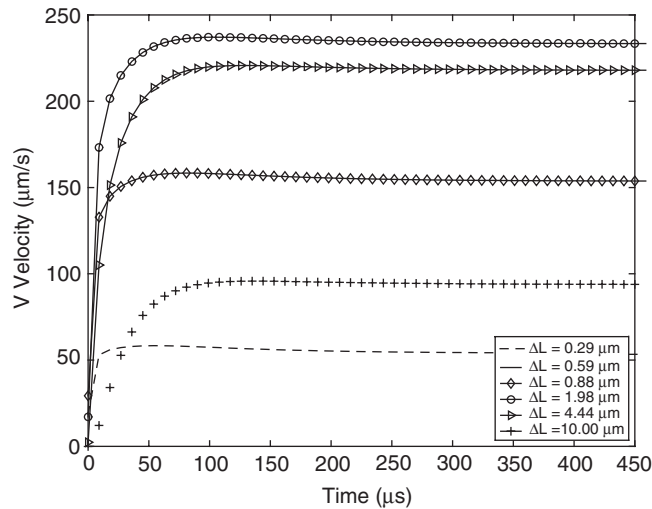


Figure 7. Evolution of V-velocity at different points along position $a - a'$ of Figure 4. ΔL denotes the distance between side channel wall and the point under consideration.

both these forces are not influenced significantly by the presence of an intersection in the channel system.

Figure 6 shows the dynamic behaviour of V-velocity at position $a - a'$ of Figure 4. Again, the flow near the wall reaches steady-state faster than the flow in the centre of the channel. In addition, the flow near the intersection reaches steady-state much more quickly compared to the flow far downstream of the intersection. Shown in Figure 7 is the evolution of the velocity at different points along position $a - a'$. The flow in the entire cross-section reaches

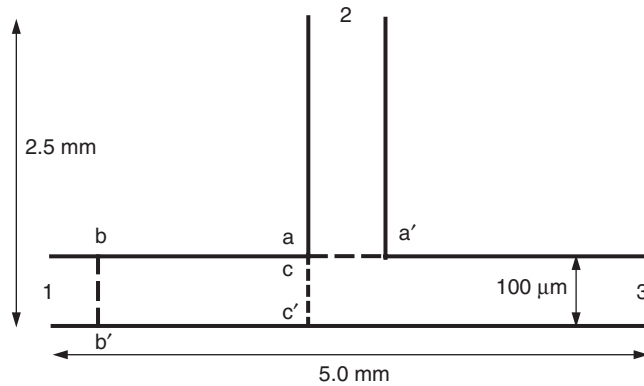


Figure 8. Geometry of a T-channel used in transient analysis.

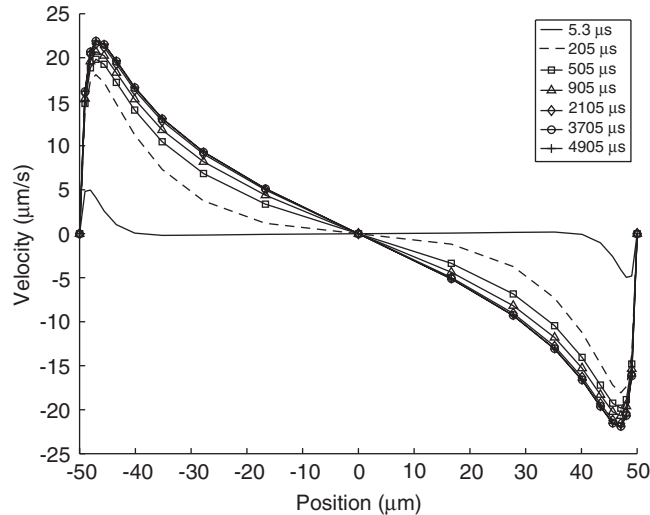


Figure 9. Evolution of V-velocity at position $a - a'$ of Figure 8.

steady-state at around $180 \mu\text{s}$ while flow at centre line of the main channel far downstream of the intersection takes about $440 \mu\text{s}$ to reach steady-state. This result is against the postulation of Reference [3] which mentions that the flow in intersection might take longer to reach steady-state than in the main channel. The reason that the flow in the intersection reaches steady-state earlier than in the main channel is that the flow near the intersection is driven mainly by an inertia force, a small pressure gradient and by electro-kinetic force, and viscous force is not as dominant as in the central part of the main channel. Since these forces act on flow in an instantaneous manner, the flow will reach steady-state much more quickly compared to the flow dominated by viscous forces.

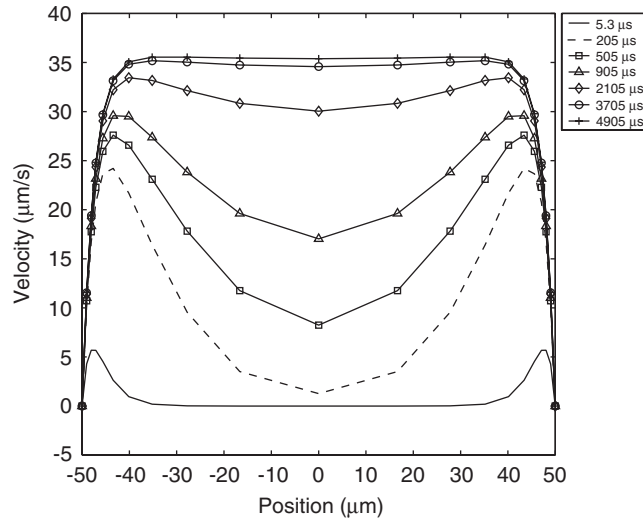


Figure 10. Evolution of U-velocity at a position far downstream of the intersection of Figure 8.

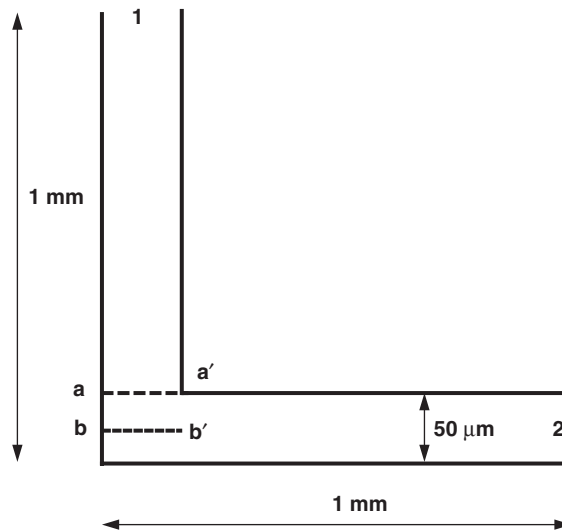


Figure 11. Geometry of an L-channel used in transient analysis.

3.3. T- and L-channel

The next case we examine is the transient behaviour of flow in a T shaped channel (see Figure 8). Initially, the fluid is at rest and at $t = 0$ s, a 257V potential is applied at reservoir 1, reservoir 3 is grounded and 128.5 V is applied at reservoir 2. The ζ -potential on all walls is set to be -1 mV. Debye length is chosen to be $2.5 \mu\text{m}$.

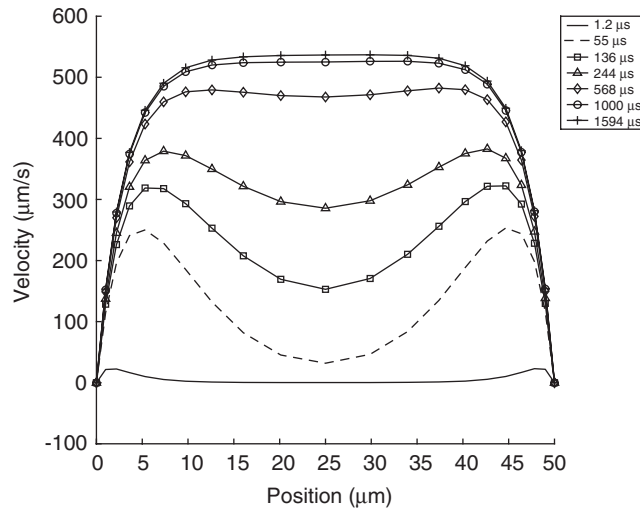


Figure 12. Evolution of U-velocity profile at a position far away from the L shape turn in the horizontal channel.

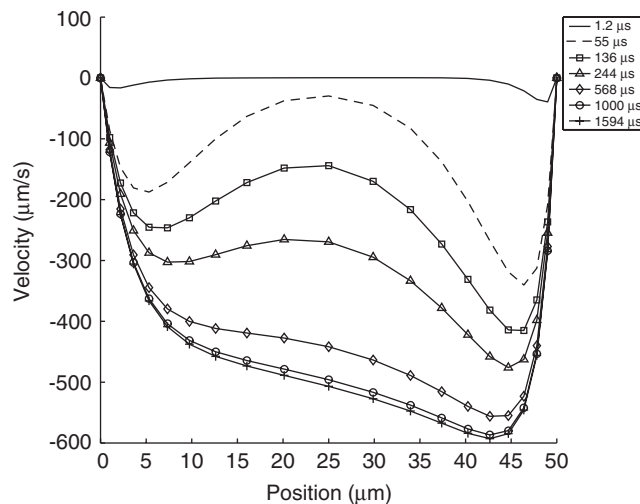


Figure 13. Evolution of V-velocity at position $a - a'$ of Figure 11.

The transient behaviour in a T-channel is similar to that observed in a cross channel. First, the time to reach steady-state varies for different positions at the same cross-section of the channel, i.e. fluid near or within the Debye layer reaches steady-state much more quickly compared to the fluid in the central part of the channel. Second, the flow in the intersection reaches steady-state much more quickly compared to the flow elsewhere. Figure 9 shows that the V-velocity at position $a - a'$ (see Figure 8) reaches steady-state after about 2 ms, while the U-velocity along the centre line at far downstream of main channel, needs about 4.9 ms to reach steady-state (see Figure 10).

The final example we investigate is the transient flow in an L shaped channel (see Figure 11). Initially, the fluid is at rest, and at $t=0$ s, a 1500 V potential is applied at reservoir 1 and reservoir 2 is grounded. The ζ -potential on all walls is set to be -1 mV. Debye length is chosen to be $3.0 \mu\text{m}$.

Figure 12 shows the development of U-velocity profiles at a position far away from the L shape turn in the horizontal channel. Figure 13 show the development of V-velocity profiles at position $a - a'$ of Figure 11. It can be seen that the transient behaviour in an L channel differs from the transient behaviour in a cross channel (and T-channel) mainly, in the fact that both U- and V-velocity develop at a similar pace. This is because the flow rate at any cross-section of the channel is the same, thus the development of U-velocity in the horizontal channel must be in accordance with the development of V-velocity in the vertical channel. This is different from the case in a cross channel since the net flow into side channel is zero in our calculation (due to balanced applied potential), and the V-velocity does not have a strict correspondence to U-velocity in main channel as it happened in the L channel.

4. NEW APPROACH FOR REDUCED-ORDER MODELLING: THEORY

4.1. Reduced-order model based on finite cloud method (FCM)

The key idea in a ROM simulation, is to express the unknowns in terms of a few global basis functions. For the electro-osmotic transport model summarized in Section 2, the unknowns are the velocities and the pressure and they will be expressed as a linear combination of global basis functions, i.e.

$$\mathbf{U}(x, y, t) = \sum_{i=1}^q \alpha_i(t) \mathbf{a}_i(x, y) \quad (8)$$

$$\mathbf{V}(x, y, t) = \sum_{i=1}^r \beta_i(t) \mathbf{b}_i(x, y) \quad (9)$$

$$\mathbf{P}(x, y, t) = \sum_{i=1}^s \gamma_i(t) \mathbf{c}_i(x, y) \quad (10)$$

Assuming the domain is discretized into n_p points, \mathbf{U} , \mathbf{V} , and \mathbf{P} are $n_p \times 1$ vectors of the x -component of the velocity, y -component of the velocity and pressure, respectively. q , r , and s are the number of modes (or the global basis) of \mathbf{U} , \mathbf{V} , and \mathbf{P} , respectively, determined to be significant. \mathbf{a}_i , \mathbf{b}_i , and \mathbf{c}_i are $n_p \times 1$ vectors denoting the i th global basis functions or modes, and α_i , β_i , and γ_i are the unknown parameters that need to be determined. The above equations can be written in a matrix form as:

$$\mathbf{U}(x, y, t) = [\mathbf{a}] \boldsymbol{\alpha} \quad (11)$$

$$\mathbf{V}(x, y, t) = [\mathbf{b}] \boldsymbol{\beta} \quad (12)$$

$$\mathbf{P}(x, y, t) = [\mathbf{c}] \boldsymbol{\gamma} \quad (13)$$

Here $[\mathbf{a}]$, $[\mathbf{b}]$ and $[\mathbf{c}]$ are $n_p \times q$, $n_p \times r$ and $n_p \times s$ matrices, respectively. Their columns are the global basis functions of \mathbf{U} , \mathbf{V} and \mathbf{P} . For example, $[\mathbf{a}] = [\mathbf{a}_1, \mathbf{a}_2, \dots, \mathbf{a}_q]$ contains the modes of \mathbf{U} . $\boldsymbol{\alpha}$, $\boldsymbol{\beta}$ and $\boldsymbol{\gamma}$ are $q \times 1$, $r \times 1$ and $s \times 1$ vectors, respectively.

The approximations in Equations (8)–(10) form the new numerical model for the solution of the electro-osmotic transport model. The solution of the electro-osmotic transport model using Equations (8)–(10), requires the calculation of the first and second derivatives of the basis functions, \mathbf{a}_i , \mathbf{b}_i , and \mathbf{c}_i . If a finite element method is used to solve the governing equations, then the derivatives of the global basis functions can be computed in a straightforward manner. Since we employ a meshless finite cloud method, the calculation of the derivatives of the global basis functions is not trivial and is explained below.

In the finite cloud method [16], an unknown quantity (e.g. the x -velocity vector \mathbf{U}) is approximated by

$$\mathbf{U} = [\mathbf{N}]\hat{\mathbf{u}} \tag{14}$$

where $[\mathbf{N}]$ is an $n_p \times n_p$ matrix referred to as the interpolation function matrix (see References [16] and [5] for more details), and $\hat{\mathbf{u}}$ is an $n_p \times 1$ vector of unknown nodal parameters. Note that the construction of $[\mathbf{N}]$ is different from the construction of the modes defined in Equations (8)–(10).

Consider, for example, the calculation of the first and second x -derivative of the basis function matrix $[\mathbf{a}]$. The first and second x -derivatives of \mathbf{U} can be expressed as:

$$\frac{\partial \mathbf{U}}{\partial x} = [\mathbf{a}_x]\boldsymbol{\alpha} = [\mathbf{N}_x]\hat{\mathbf{u}} \tag{15}$$

$$\frac{\partial^2 \mathbf{U}}{\partial x^2} = [\mathbf{a}_{xx}]\boldsymbol{\alpha} = [\mathbf{N}_{xx}]\hat{\mathbf{u}} \tag{16}$$

Here $[\mathbf{a}_x]$ and $[\mathbf{a}_{xx}]$ are $n_p \times q$ matrices that contain the first and second x -derivatives, respectively, of the basis functions. Similarly, $[\mathbf{N}_x]$ and $[\mathbf{N}_{xx}]$ are $n_p \times n_p$ matrices that contain the first and second x -derivatives, respectively, of the interpolation function matrix $[\mathbf{N}]$ (see e.g. Reference [5] for construction of these matrices). From Equations (11) and (14) we have

$$\mathbf{U} = [\mathbf{N}]\hat{\mathbf{u}} = [\mathbf{a}]\boldsymbol{\alpha} \tag{17}$$

Combining Equations (15)–(17), $[\mathbf{a}_x]$ and $[\mathbf{a}_{xx}]$ can be computed by

$$[\mathbf{a}_x] = [\mathbf{N}_x][\mathbf{N}]^{-1}[\mathbf{a}] \tag{18}$$

$$[\mathbf{a}_{xx}] = [\mathbf{N}_{xx}][\mathbf{N}]^{-1}[\mathbf{a}] \tag{19}$$

The derivatives of other global basis matrices, $[\mathbf{b}]$ and $[\mathbf{c}]$, can be computed in a similar manner.

Since the electro-kinetic equations (Equations (1) and (2)) are decoupled from the flow equations (Equations (3) and (4)), we first solve the Poisson–Boltzman equation and the Laplace equation to get the body force through Equation (5). Then the Navier–Stokes equations are solved to compute the velocities and pressure. The solution of the Poisson–Boltzmann equation and the Laplace equation accounts for a small fraction of the total computational

cost. The Navier–Stokes equations are solved by the reduced-order modelling approach using a fractional-step method (see Reference [5] for details on the fractional-step method). The fractional-step method includes three sub-steps, i.e. a predictor step to calculate an intermediate velocity \mathbf{U}^* , an intermediate step to solve for the pressure field and a corrector step to enforce the continuity condition to determine the new velocity field. Each of these steps gives rise to a matrix problem to compute the unknown parameters α_i , β_i , and γ_i . The matrix problems in these steps are, however, over-determined, i.e. we have more equations and few unknowns. Galerkin conditions are enforced in each of the three steps to solve the resulting linear systems. Details on the solution of the Navier–Stokes equations using the global basis functions can be found in Appendix A.

4.2. Generation of basis functions

4.2.1. Weighted Karhunen–Loève decomposition. The basis functions in a reduced-order modelling approach can be generated using various techniques [8, 9, 17]. Of these techniques, Karhunen–Loève (KL) decomposition (also referred to as proper orthogonal decomposition (POD) in some literature [8]) has been widely used in many applications, e.g. turbulent flow analysis [17], hydrodynamic stability analysis [8], dynamic control in various fields (mechanical systems [10], fluid flow [18, 19] and chemical reactions [20, 21]), heat transfer [22] and recently MEMS device simulation [7, 23].

The key idea in a KL decomposition approach is to choose certain basis such that the observed behaviour of the system can be represented by the smallest linear subspace spanned by them [11, 24]. The ‘observed behaviour of the system’ is usually represented by a number of snapshots of variables taken during the dynamic process of the system. Thus, finding N such orthogonal basis functions is equivalent to choosing $\{\mathbf{a}_1, \dots, \mathbf{a}_N\}$ to minimize:

$$\sum_{i=1}^{N_s} |\mathbf{u}_i - \text{proj}(\mathbf{u}_i, \text{span}\{\mathbf{a}_1, \dots, \mathbf{a}_N\})|^2 \quad (20)$$

Here \mathbf{u}_i is the $n_p \times 1$ vector of the i th snapshot information and N_s is the number of snapshots. It has been proven in Reference [7] that a set of basis $\{\mathbf{a}_1, \dots, \mathbf{a}_N\}$ are simply the column vectors of matrix \mathbf{L} which is obtained by doing a singular value decomposition (SVD) of the snapshot ensemble matrix $\tilde{\mathbf{U}}$:

$$[\tilde{\mathbf{U}}] = \mathbf{L}\mathbf{\Sigma}\mathbf{R}^T \quad (21)$$

where $\tilde{\mathbf{U}}$ is the matrix containing the snapshot information:

$$[\tilde{\mathbf{U}}] = [\mathbf{u}_1, \mathbf{u}_2 \cdots \mathbf{u}_{N_s}] \quad (22)$$

In this paper, we introduce a weighted KL decomposition technique to generate the basis functions. The concept of using weights in a KL decomposition approach has been suggested before [21]. The idea is that instead of trying to minimize Equation (20), we assign different weights to different snapshots and try to minimize the weighted residual, i.e.

$$\sum_{i=1}^{N_s} |w_i \mathbf{u}_i - \text{proj}(w_i \mathbf{u}_i, \text{span}\{\mathbf{a}_1, \dots, \mathbf{a}_N\})|^2 \quad (23)$$

Observe the difference between Equations (20) and (23). w_i is the weighting assigned to snapshot \mathbf{u}_i . In the weighted KL approach, instead of minimizing a least-squares measure of

'error' between the linear subspace spanned by the basis functions and the observation space, we minimize the weighted 'error' between these two spaces.

By using the fact that SVD of snapshot ensemble gives the basis which minimizes Equation (20), it is easy to show that the basis which minimizes Equation (23) is the column vector of matrix \mathbf{L}_2 :

$$\tilde{\mathbf{U}}\mathbf{W} = \mathbf{L}_2\mathbf{\Sigma}_2\mathbf{R}_2^T \quad (24)$$

Where \mathbf{W} is an $N_s \times N_s$ diagonal matrix whose diagonal elements are the weighting coefficients for each snapshot, i.e. $[\mathbf{W}]_{i,i} = w_i$.

Remarks

1. If the weighting function matrix is identity, i.e. $w_i = 1$ ($i = 1, 2, \dots, N_s$), then the weighted KL technique and the standard KL technique produce identical basis.
2. In the implementation of the weighted KL technique, once the snapshots are obtained, a weight is assigned to each snapshot.
3. Since the snapshot ensemble matrix is multiplied by a diagonal matrix, the computational cost of a weighted KL decomposition based on (24) is almost the same as the computational cost of the classical KL decomposition based on (21).
4. The x -velocity basis $[\mathbf{a}_1, \mathbf{a}_2, \dots, \mathbf{a}_q]$ is computed by considering weighted snapshots of x -velocity, i.e. $\tilde{\mathbf{U}} = [w_1\mathbf{u}_1, w_2\mathbf{u}_2, \dots, w_{N_s}\mathbf{u}_{N_s}]$, where \mathbf{u}_i is the $n_p \times 1$ vector of x -velocity and w_i is the weighting assigned to the i th snapshot. An SVD of $\tilde{\mathbf{U}}$ gives $\tilde{\mathbf{U}} = \mathbf{L}_2\mathbf{\Sigma}_2\mathbf{R}_2^T$ and the first q columns of \mathbf{L}_2 are the global basis $[\mathbf{a}_1, \mathbf{a}_2, \dots, \mathbf{a}_q]$. The y -velocity basis $[\mathbf{b}_1, \mathbf{b}_2, \dots, \mathbf{b}_r]$ and the pressure basis $[\mathbf{c}_1, \mathbf{c}_2, \dots, \mathbf{c}_s]$ are computed in a similar manner.

4.2.2. Significance of weighting. The concept of assigning different weights to different snapshots is useful when the transient behaviour of certain variables (for example, velocity or pressure) changes significantly with time. For example, in the case of electro-osmotic transport, the flow gets to steady-state at different times for different locations in the channel (this has already been discussed in Section 3.2 and 3.3). If a higher weighting is assigned to those snapshots taken during the fast-changing transient, then the basis obtained with SVD will, according to Equation (23), be able to produce more accurate results. In other words, the new basis obtained with weighted snapshots will be able to represent the system behaviour much better compared to the basis functions obtained with the classical KL decomposition technique. If the transient behaviour of the system is gradual, then the use of the weighting function is limited and both weighted and classical KL decomposition techniques can be expected to produce comparable accuracy results.

A feasible approach for rapidly varying transient solutions is to obtain more snapshots during the time when the solution is changing rapidly and to compute the basis using the classical KL decomposition technique. However, there are several situations when obtaining snapshots is not straight-forward. For example, when snapshots are obtained from experiments, repeating the experiment to obtain more snapshots can be very expensive. Similarly, if the snapshots are obtained from numerical simulations and if a rapidly varying transient is represented by a few snapshots, repeating the simulation to get more snapshots with a smaller time step can be very expensive. A good compromise in such cases is to use weighted snapshots, to get better basis functions, instead of repeating the experiments or the numerical simulations. Many

times it is difficult to foresee the various time scales encountered in the system. The concept of weighting in a KL decomposition technique introduces more flexibility and accuracy to represent multiple time scales in a dynamical system.

4.2.3. Discussion on weighted basis versus error in the solution. It is important to note that weighting is a concept introduced to improve the accuracy over certain time scales or periods rather than a technique that can be used to improve the accuracy over the entire time period. In fact, reduced-order modelling using weighted basis usually exhibits slightly higher error in the time period which is less-significantly weighted. Typically, reduced-order modelling exhibits a very non-uniform error in the whole time domain, i.e. it might behave very well in certain time periods but not be able to capture the basic characteristics in certain other time periods. By using a weighted KL basis, it is possible to achieve a more uniform reduction in error in the solution.

A second question of significant interest is how does a weighted basis compare with other basis in capturing the system transient? There is no easy answer without a detailed mathematical analysis. However, we do know that (i) increasing the number of basis functions used in approximating the velocities and pressure generally improves the accuracy of the simulation, (ii) different methods generate different basis and the number of significant basis functions that need to be included in each method is different. The accuracy of the solution is influenced by both the number of basis and the quality of basis. In our results, we have observed that the number of basis that need to be included in a weighted approach is less than the number of basis that need to be included in the classical KL approach for comparable accuracy.

5. REDUCED-ORDER MODELLING: RESULTS

The simplest electro-kinetic geometry is a straight channel and a reduced-order model, using only a few modes, can be generated using weighted and standard KL decomposition techniques [23]. In this section, we present results for more complicated geometries—namely, a cross channel, a T-channel and an L channel.

5.1. Cross channel

The cross channel geometry considered for transient analysis is shown in Figure 4. The cross channel is an interesting problem as the flow in the intersection exhibits many interesting characteristics. In the case of balanced applied potentials, the net flow into the side channel is negligible but the fluid velocity does not vanish in the side channel [5]. A good reduced-order model (ROM) should capture both the flow in the main channel and flow within the intersection of the cross channel. As discussed in Section 3.2, the flow in the cross channel exhibits multiple time scales, i.e. the flow within the intersection steady-state much more quickly compared to the flow in the main channel. In addition, the velocity profile within the intersection is more complex compared to the velocity profile in the main channel. To capture the multiple time scales encountered in the cross channel example, a weighted KL decomposition is used to generate the basis functions for ROM.

Sixty snapshots are used to generate a reduced-order model. The snapshots are equi-spaced in time with a time period of 8.85 μs between snapshots. Figure 14 shows the weighting

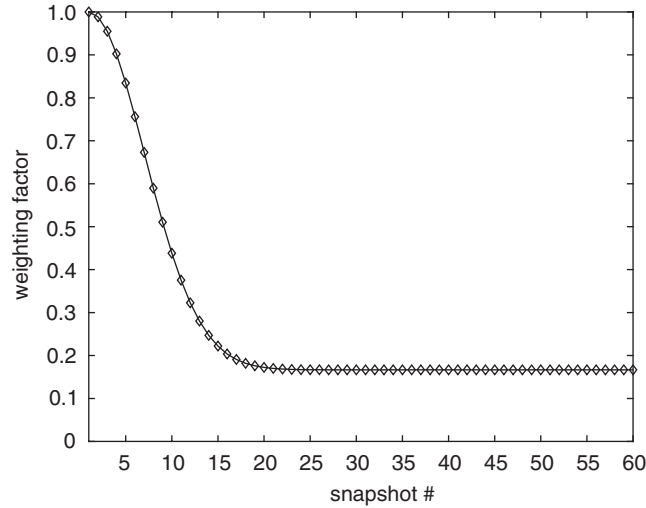


Figure 14. A weighting function that assigns different weighting coefficients for different snapshots.

function employed to generate the weighted KL basis. The weighting coefficient, $w(i)$, for the i th snapshot is calculated by

$$w(i) = r + (1 - r) \frac{e^{-(i/c)^2} - e^{-(N_s/c)^2}}{1 - e^{-(N_s/c)^2}} \quad (25)$$

where N_s is the total number of snapshots, r is the minimal weighting for all snapshots, and c is a parameter controlling the steepness of the weighting function. In this calculation, since the first few snapshots contain the information of how V-velocity near the intersection reaches steady-state, they are weighted more heavily compared to the other snapshots. The snapshots closer to the steady-state value are not critical, so they are assigned a lower weighting. The minimal weighting is set to be $\frac{1}{6}$. The steepness parameter is chosen to be 8.5 in this case.

ROM simulations for the cross channel were performed with all initial and boundary conditions as described in Section 3.2. Figure 15 shows the U-velocity prediction in the main channel and both methods (standard and weighted KL techniques) produce almost identical results at steady-state, though ROM using weighted KL basis gives slightly better accuracy at the beginning of the simulation.

In Figure 16, we compare the performance of weighted and standard KL techniques by fixing the number of snapshots and investigating the number of basis required with each technique to get comparable accuracy. We use 60 snapshots in both approaches. For the weighted KL technique we use 4 basis functions for the x -component of the velocity, 4 basis functions for the y -component of the velocity and 3 basis functions for the pressure (referred to as 4U+4V+3P in Figure 16). To reproduce the results obtained by the weighted KL technique, we had to use 6 basis functions for the x -velocity, 6 basis functions for the y -velocity and 6 basis functions for the pressure (denoted as 6U + 6V + 6P). For comparable accuracy, we need almost twice the number of basis functions in a standard KL approach compared to the weighted KL technique. This result indicates that when the number of snapshots is fixed, a weighted KL technique needs fewer basis functions compared to a standard KL technique to

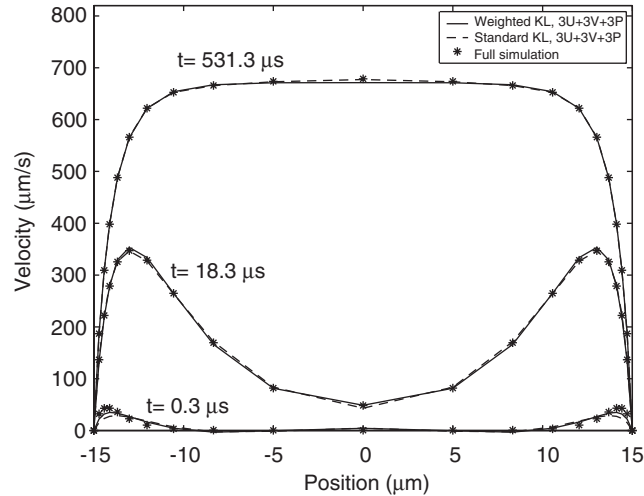


Figure 15. Comparison of U-velocity in the main channel far upstream of the intersection. 60 snapshots are used and $3U + 3V + 3P$ basis are used in both methods.

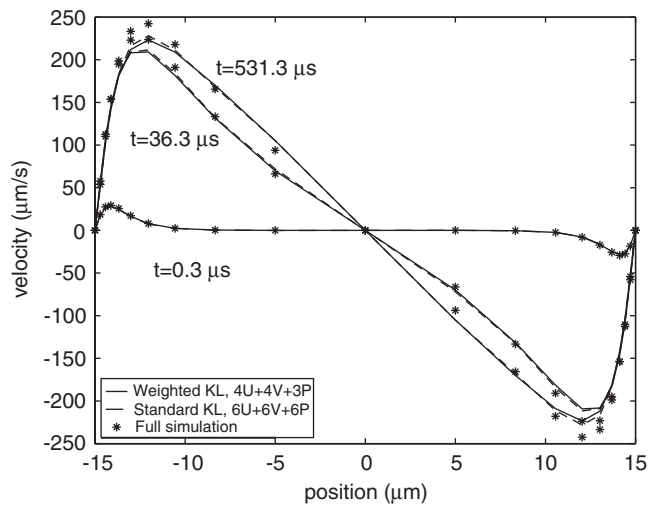


Figure 16. Comparison of V-velocity at position $a - a'$ of Figure 4. 60 snapshots are used in both methods.

reproduce full simulation results. The use of less basis functions leads to a computationally more efficient approach. Table I compares the speedup factors obtained with different numbers of basis for U, V and P. It can be observed that a ROM technique with $4U + 4V + 3P$ basis is almost twice as fast as the ROM technique with $6U + 6V + 6P$ basis, i.e. a ROM based on weighted KL technique can be twice as fast as the ROM based on standard KL technique while achieving essentially the same accuracy.

Table I. Performance comparison of ROM simulation for different situations

Method	Number of unknowns	Computation time (s)	Speedup factor
Finite cloud method	7875	6558.1	1.0
ROM, 3U + 3V + 3P basis	9	168.5	38.9
ROM, 4U + 4V + 3P basis	11	236.5	27.7
ROM, 6U + 6V + 6P basis	18	468.5	14.0

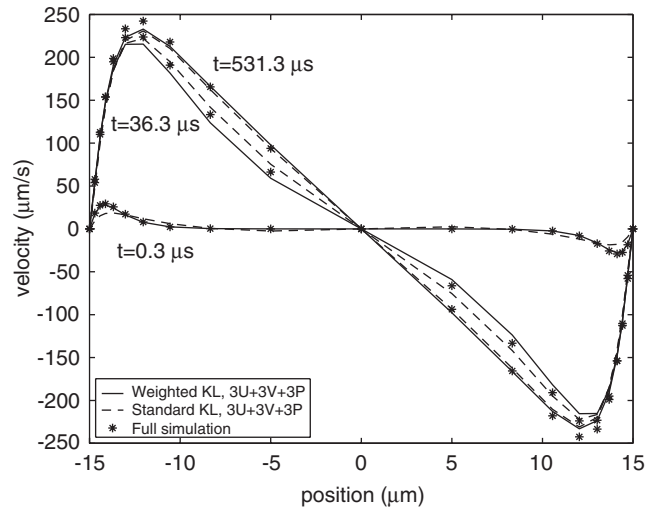


Figure 17. Comparison of V-velocity at position $a - a'$ of Figure 4. 20 snapshots and 3U + 3V + 3P basis are used in both ROM techniques.

In Figure 17, we compare the performance of weighted and standard KL techniques by fixing the number of snapshots and basis functions. The number of snapshots is fixed to 20 and the number of basis functions for U, V and P are fixed to 3, i.e. 3U + 3V + 3P. The snapshots are equi-spaced in time with a time period of 26.6 μs between snapshots. The weighting coefficients for the weighted KL technique are computed by using Equation (25). The minimal weighting r is $\frac{1}{6}$ and the steepness parameter is set to be 9. Figure 17 compares the weighted and standard KL techniques with the full transient simulation. The results indicate that the weighted KL basis is able to capture the velocity profile during the initial transient much more effectively compared to the standard KL approach. The steady-state solution predicted by both techniques is almost the same and compares well with the full transient simulation. From this we can conclude that with the same number of snapshots and basis functions, the weighted KL approach can offer better accuracy in resolving multiple time scales compared to the standard KL approach.

In Figure 18, we compare the performance of weighted and standard KL techniques by fixing the number of basis functions (3U + 3V + 3P) and using different snapshots with each approach. The weighted KL method uses 22 snapshots to generate the basis functions (the weighting coefficients are again selected by the approach described in the previous paragraph)

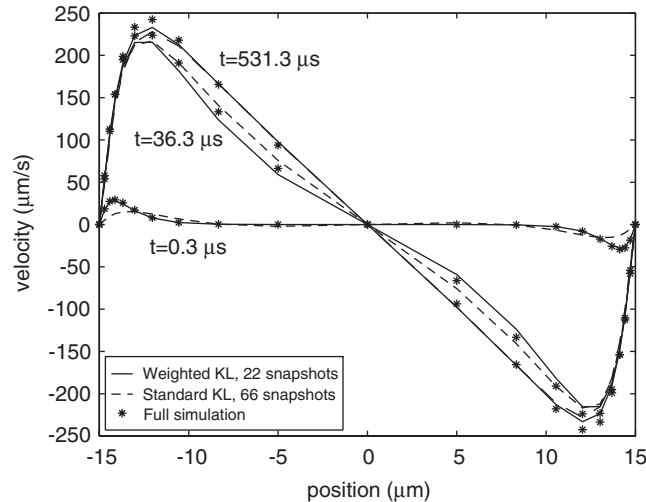


Figure 18. Comparison of V-velocity at position $a - a'$ of Figure 4. $3U + 3V + 3P$ basis are used in both ROM techniques. 22 snapshots are used in the weighted KL method and 66 snapshots are used in the standard KL method to generate basis functions.

and the standard KL method uses 66 snapshots to generate basis functions. The result in Figure 18 indicates that the weighted KL technique offers better accuracy during the initial transient compared to the standard KL method, while both methods produce comparable accuracy at steady-state. From this result, we can conclude that for a fixed number of basis functions, a weighted KL technique using less number of snapshots can produce better accuracy compared to a standard KL technique.

5.2. T-channel

The T-channel geometry considered here is shown in Figure 8. Just like the cross-channel example, the flow near the intersection of the main channel and the side channel is complex in a T-junction. The flow in the intersection gets to steady-state much more quickly compared to the flow in the main channel. The multiple time scales encountered in the T-channel example can again be captured much more effectively by using the weighted KL technique.

We consider two snapshot cases with both weighted and standard KL techniques. Figure 19 shows the weighting function employed for the snapshots in the weighted KL technique when 22 snapshots are used. The snapshots are equi-spaced in time with a time period of $295.5 \mu\text{s}$ between snapshots. The first few snapshots are weighted heavily since the transient behaviour of V-velocity near the intersection lies mainly in these snapshots. The minimal weighting r is $\frac{1}{6}$, and the steepness parameter c is set to be 2.5. When 66 snapshots are used in generating basis functions, the weighting coefficients are calculated using Equation (25) with the minimal weighting r and steepness parameter c set to be $\frac{1}{7}$ and 2.5, respectively. ROM simulations were done with all initial and boundary conditions as described in Section 3.3.

In Figure 20, we compare the performance of weighted and standard KL techniques by fixing the number of snapshots to 22 and the basis to 3, i.e. we use 3 basis functions for U-velocity, 3 basis functions for V-velocity and 3 basis functions for pressure (denoted as

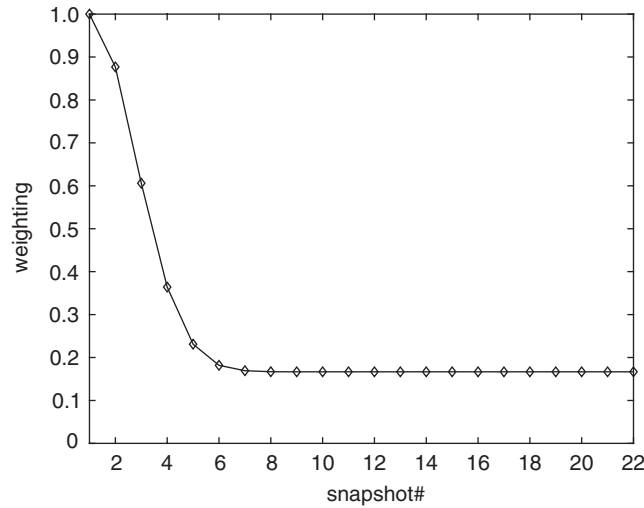


Figure 19. A weighting function that assigns different weighting coefficients for different snapshots (22 snapshots are used).

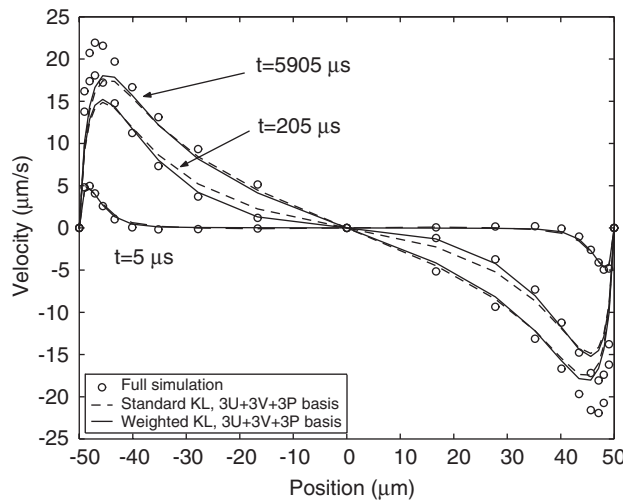


Figure 20. Comparison of V-velocity at position $a - a'$ of Figure 8. 22 snapshots are used and $3U + 3V + 3P$ basis functions are used in both methods.

$3U + 3V + 3P$). From Figure 20, we can observe that the weighted KL technique does a better job in capturing the initial transient, i.e. in the time period where the snapshots are weighted heavily.

In Figure 21, we compare the performance of weighted and standard KL techniques by fixing the number of basis functions ($3U + 3V + 3P$) and using different snapshots with each approach. We use 22 snapshots in the weighted KL technique and 66 snapshots in the standard

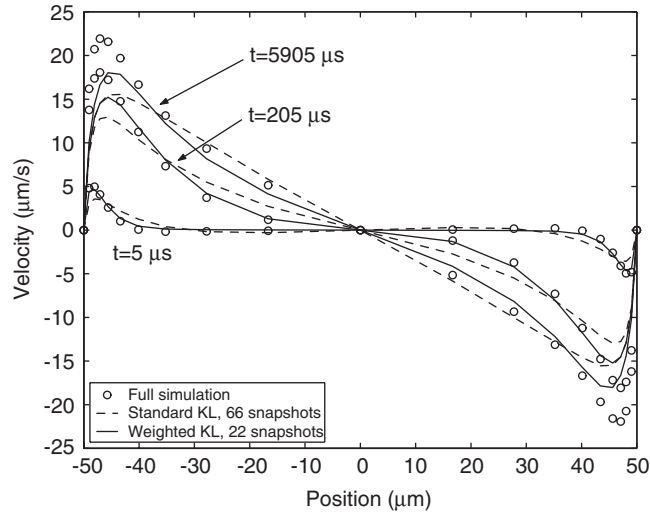


Figure 21. Comparison of V-velocity at position $a-a'$ of Figure 8. $3U+3V+3P$ basis functions are used in both methods.

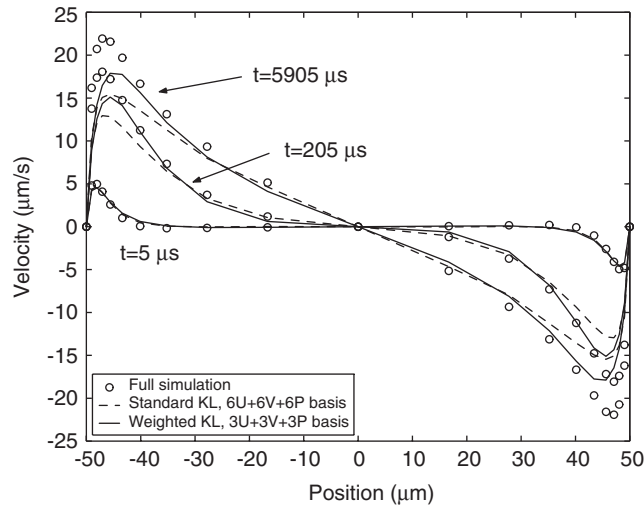


Figure 22. Comparison of V-velocity at position $a-a'$ of Figure 8. 66 snapshots are used in both methods.

KL approach. We observe that the weighted KL approach performs better compared to the standard KL approach even though the standard KL approach included more snapshots. The result in Figure 21 demonstrates that a weighted KL technique with fewer snapshots can be more accurate and computationally more efficient compared to a standard KL technique.

In Figure 22, we compare the performance of weighted and standard KL techniques by fixing the number of snapshots and investigating the number of basis required with each

approach to get a desirable accuracy. We use 66 snap shots in both approaches. For the weighted KL technique, we use 3 U-velocity, 3 V-velocity and 3 pressure basis functions. For the standard KL technique, we use 6 U-velocity, 6 V-velocity and 6 pressure basis functions. In spite of more basis functions in the standard KL approach, we observe from Figure 22 that the weighted KL technique exhibits better accuracy compared to the standard KL technique. This result demonstrates that a weighted KL technique can produce better accuracy with fewer basis functions compared to a standard KL technique. Fewer basis functions also makes the weighted KL technique computationally more efficient.

Even though the weighted KL technique performs better compared to the standard KL technique, both these methods fail to capture the steady-state V-velocity in the intersection (see e.g. Figure 22). The ROM solution can be improved by considering two approaches: First, inclusion of more critical snapshots and basis functions can improve the accuracy of the solution. Second, and more significantly, in our current approach the U, V and P basis are computed by a decoupled approach, i.e. the U basis is constructed by considering snapshots of U-velocity, the V-basis is constructed by considering snapshots of V-velocity and the pressure basis by considering snapshots of pressure alone. The flow in the intersection is complicated and a coupled approach can generate more accurate results. In a coupled approach, the basis is computed by considering the snapshots of U-velocity, V-velocity and pressure all at once. The coupled approach to generate basis functions can, however, be more expensive compared to the decoupled approach.

5.3. *L-channel*

The L-channel considered here is shown in Figure 11. The primary difference between the flow characteristics in an L-channel compared to the flow in a cross or a T-channel is that in an L-channel the flow evolves to steady-state at the same pace in both the main channel and in the intersection (see Figures 12 and 13). Also, as shown in Figure 13, the velocity approaches steady-state in a much gradual way, and this is very different from the situation in T and cross channel where V-velocity near the intersection approaches steady-state very quickly.

We compare the weighted and standard KL techniques for the L-channel by using 21 snapshots to generate the basis functions. The snapshots are equi-spaced in time with a time period of $81.0 \mu\text{s}$ between them. The minimal weighting r , in Equation (25) is set to be $\frac{1}{6}$ and the steepness parameter c is set to be 2.5. Figure 23 shows a comparison of V-velocity obtained by both techniques. 3 U-velocity, 3 V-velocity and 3 pressure basis are used in both techniques. It can be observed that both approaches produce almost identical results. When the transient behaviour is gradual or when the time scales in the problem are fairly constant, the accuracy obtained by both techniques is very similar. The ROM result in Figure 23 does not match very well with the full simulation results during the initial transient. The ROM result can be improved by including more basis functions. By considering 6 U-velocity, 6 V-velocity, and 6 pressure basis, we show in Figure 24 that both reduced-order modelling techniques can match the full simulation results.

5.4. *Prediction of flow using reduced-order modelling*

In Sections 5.1–5.3, the ROM technique was used to reconstruct the full simulation results using a few basis functions obtained from the weighted KL decomposition. The more useful

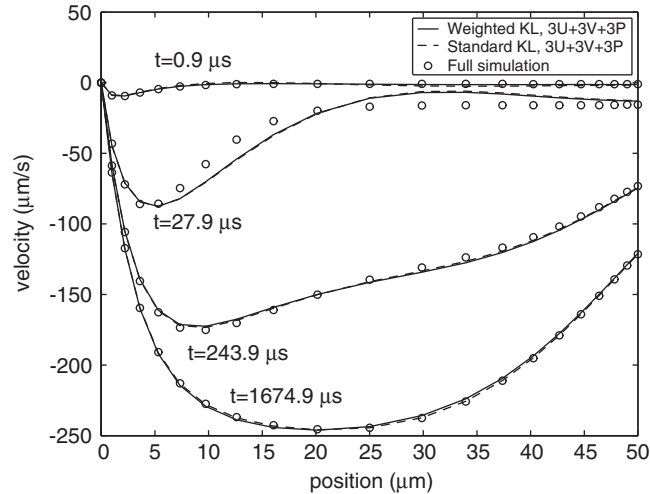


Figure 23. Comparison of V -velocity at position $b - b'$ of Figure 11. 21 snapshots are used for basis function generation. 3U, 3V and 3P basis are used in both techniques.

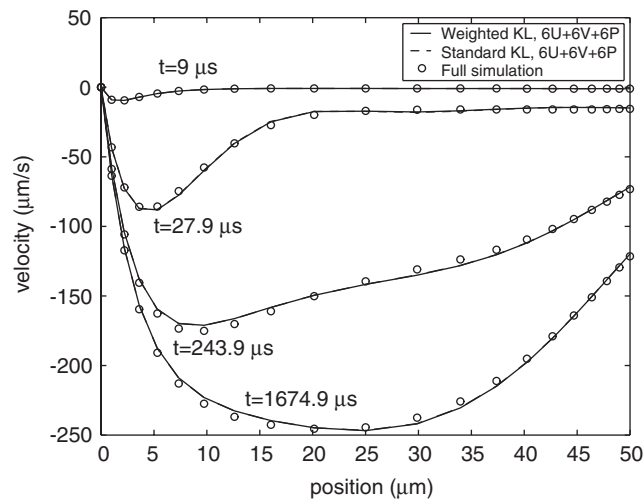


Figure 24. Comparison of V -velocity at position $b - b'$ of Figure 11. 21 snapshots are used for basis function generation. 6U, 6V and 6P basis are used in both techniques.

aspect of the ROM technique is to predict the flow characteristics at states far away from the decomposition state where the basis has been obtained. In Section 5.3, ROM was used to study the flow characteristics in an L channel when the flow evolved from the stagnant state to the steady-state. The scenario we consider here is the evolution of flow from the previous steady-state to a stagnant state. Specifically, the initial velocity field is taken from the steady-state solution obtained in Section 3.3, and the applied voltage at reservoir 1 in Figure 11 is set to zero at $t = 0$ s. 6 basis for U -velocity, 6 basis for V -velocity and 6 basis for pressure obtained

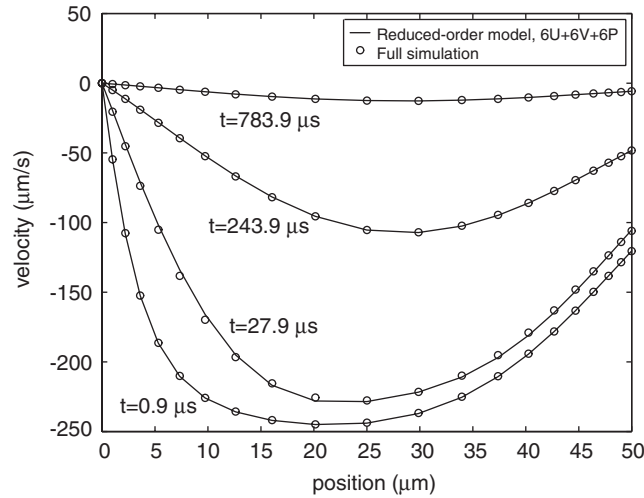


Figure 25. Comparison of V-velocity at position $b - b'$ of Figure 11. 21 snapshots are used for basis function generation. 6U, 6V and 6P basis are used in ROM.

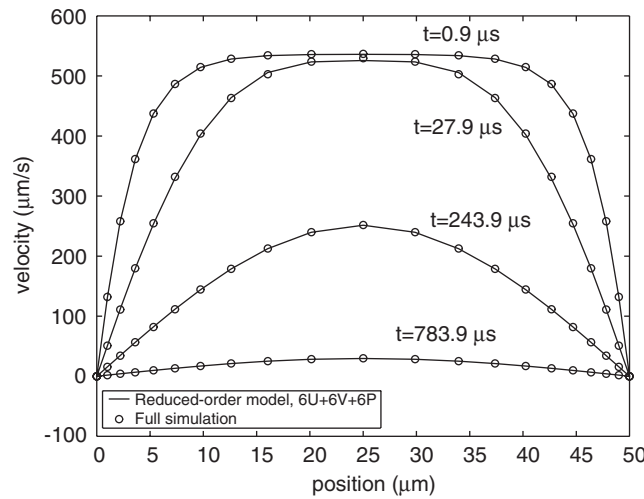


Figure 26. Comparison of V-velocity at position far away from the L shape turn in the horizontal channel of Figure 11. 21 snapshots are used for basis function generation. 6U, 6V and 6P basis are used in ROM.

in Section 5.3 using 21 weighted snapshots are used in the ROM simulation. Figure 25 shows the comparison of velocity evolution at position $b - b'$ (see Figure 11) obtained by full simulation and ROM. Figure 26 shows the comparison of velocity profile evolution at position far away from the L shape turn in the horizontal channel. The ROM predictions agree very well with the full simulation results at both locations. This result indicates that the weighted

KL decomposition technique can be used effectively to capture flow characteristics at states far away from the decomposition state.

6. CONCLUSIONS

In this paper, the transient behaviour of electro-osmotic transport is studied in several typical electrokinetic geometries. A meshless semi-implicit-multi-step (SIMS) technique is employed to simulate the electro-osmotic transport model. The time needed for the flow to reach steady-state is different for different positions across the channel width. Specifically, the flow near the wall reaches steady-state much more quickly compared to the flow along the centre line of the channel. Simulations also show that, for balanced applied potentials, the flow within the intersection of a cross or a T-channel reaches steady-state much more quickly compared to the flow along the centre line of the main channel.

A reduced-order modelling technique that uses a weighted Karhunen–Loève (KL) decomposition technique to compute global basis functions is proposed in this paper. The basic idea in a weighted KL technique is to assign a weight to each snapshot. The global basis functions are computed by taking the singular value decomposition (SVD) of the matrix containing the weighted snapshots. In the reduced-order model, the unknown quantities are approximated in terms of the global basis functions and a SIMS technique is used to solve the Navier–Stokes equations in the electro-osmotic transport model. We have shown that the reduced-order modelling technique based on the weighted KL decomposition is computationally more efficient and can capture the multiple time scales encountered in electro-osmosis much more effectively compared to the reduced-order modelling technique based on the standard KL decomposition technique. We have also shown that ROM technique can be used effectively to predict the flow characteristics at a state away from the decomposition state where the global basis have been extracted.

APPENDIX A: SOLUTION OF NAVIER–STOKES EQUATIONS USING GLOBAL BASIS FUNCTIONS

A semi-implicit multi-step (SIMS) algorithm is used to solve the Navier–Stokes equation (details of the algorithm can be found in a previous paper [5]). The difference between a full simulation and a reduced-order model is that, the unknowns \mathbf{U} , \mathbf{V} and \mathbf{P} are now expressed in term of the global basis functions \mathbf{a}_i , \mathbf{b}_i , and \mathbf{c}_i . Here we describe how to implement the SIMS algorithm by using the global basis functions.

The first step (see Reference [5]) of SIMS algorithm calculates the intermediate velocity \mathbf{U}^* , \mathbf{V}^* :

$$\mathbf{U}_i^* = \mathbf{U}_i^n + \Delta t \left(\frac{1}{Re} \nabla^2 \mathbf{U}_i^* - \mathbf{U}_i^n \frac{\partial \mathbf{U}_i^*}{\partial x} - \mathbf{V}_i^n \frac{\partial \mathbf{U}_i^*}{\partial y} + \mathbf{F}_{x_i}^n \right) \quad (\text{A1})$$

$$\mathbf{V}_i^* = \mathbf{V}_i^n + \Delta t \left(\frac{1}{Re} \nabla^2 \mathbf{V}_i^* - \mathbf{U}_i^n \frac{\partial \mathbf{V}_i^*}{\partial x} - \mathbf{V}_i^n \frac{\partial \mathbf{V}_i^*}{\partial y} + \mathbf{F}_{y_i}^n \right) \quad (\text{A2})$$

By substituting the global approximations for \mathbf{U} and \mathbf{V} into Equations (A1) and (A2), we get

$$[\mathbf{K}_{u1}] \boldsymbol{\alpha}^* = \mathbf{U}^n + \Delta t \mathbf{F}_x^n \tag{A3}$$

$$[\mathbf{K}_{v1}] \boldsymbol{\beta}^* = \mathbf{V}^n + \Delta t \mathbf{F}_y^n \tag{A4}$$

where \mathbf{K}_{u1} and \mathbf{K}_{v1} are of size $n_p \times q$ and $n_p \times r$, respectively. The i th rows of \mathbf{K}_{u1} and \mathbf{K}_{v1} are given by

$$[\mathbf{K}_{u1}]_{ij} = [\mathbf{a}]_{ij} + \Delta t \left(\mathbf{U}_i^n [\mathbf{a}_x]_{ij} + \mathbf{V}_i^n [\mathbf{a}_y]_{ij} - \frac{1}{Re} ([\mathbf{a}_{xx}]_{ij} + [\mathbf{a}_{yy}]_{ij}) \right) \quad j = 1, 2, \dots, q \tag{A5}$$

$$[\mathbf{K}_{v1}]_{ij} = [\mathbf{b}]_{ij} + \Delta t \left(\mathbf{U}_i^n [\mathbf{b}_x]_{ij} + \mathbf{V}_i^n [\mathbf{b}_y]_{ij} - \frac{1}{Re} ([\mathbf{b}_{xx}]_{ij} + [\mathbf{b}_{yy}]_{ij}) \right) \quad j = 1, 2, \dots, r \tag{A6}$$

Here $[\mathbf{a}_x]$, $[\mathbf{a}_{xx}]$, $[\mathbf{a}_{yy}]$, $[\mathbf{b}_x]$, $[\mathbf{b}_{xx}]$ and $[\mathbf{b}_{yy}]$ are various derivatives of the global basis functions and they are computed as described in Section 4.1. $[\mathbf{K}_{u1}]_{ij}$ refers to the i th row and j th column entry of matrix $[\mathbf{K}_{u1}]$.

The matrix problems in Equations (A3) and (A4) are over-determined and cannot be solved directly. To obtain a good solution, the error in the governing equation is made orthogonal to the basis functions used to construct the low-order model. This Galerkin condition ensures that the solution obtained is the best possible solution using the few number of modes retained from the SVD. The orthogonality condition is enforced by a Galerkin projection of the matrix problems (A3) and (A4) onto $[\mathbf{a}]$ and $[\mathbf{b}]$, respectively:

$$\left(\int_V \mathbf{a}_i^T [\mathbf{K}_{u1}] dV \right) \boldsymbol{\alpha}^* = \int_V \mathbf{a}_i^T (\mathbf{U}^n + \Delta t \mathbf{F}_x^n) dV \quad i = 1, 2, \dots, q \tag{A7}$$

$$\left(\int_V \mathbf{b}_i^T [\mathbf{K}_{v1}] dV \right) \boldsymbol{\beta}^* = \int_V \mathbf{b}_i^T (\mathbf{V}^n + \Delta t \mathbf{F}_y^n) dV \quad i = 1, 2, \dots, r \tag{A8}$$

The integrals in the above equations can be computed by a Nyström technique [25]. For example,

$$\int_V \mathbf{a}_i^T \mathbf{F} dV \approx \sum_{j=1}^{n_p} [\mathbf{a}_i^T]_j [\mathbf{F}]_j \Delta V_j \tag{A9}$$

where ΔV_j is the nodal volume associated with node j (see Reference [16] for details). The matrix problems in Equations (A7) and (A8) are now square and can be solved by an iterative or a direct solver. Other steps of the SIMS algorithm can be implemented in a similar manner [26].

Since we apply homogeneous boundary conditions (Dirichlet or Neumann type) for \mathbf{U} , \mathbf{V} and \mathbf{P} , the basis functions obtained through the KL decomposition (or weighted KL decomposition) of the snapshot ensemble matrix automatically satisfy the boundary conditions. Thus boundary conditions are enforced automatically in the reduced-order model.

ACKNOWLEDGEMENTS

This work is supported by a grant from DARPA under agreement number F30602-98-2-0718 and by an NSF CAREER award to Dr Aluru. We thank the anonymous reviewer for bringing References [20] and [21] to our attention.

REFERENCES

- Harrison DJ, Fluri K, Seiler K, Fan Z, Effenhauser CS, Manz A. Micromachining a miniaturized capillary electrophoresis-based chemical analysis system on a chip. *Science* 1993; **261**:895–897.
- Manz A, Becker H. *Microsystem Technology in Chemistry and Life Sciences*. Springer: Berlin, Heidelberg, 1999.
- Patankar NA, Hu HH. Numerical simulation of electro-osmotic flow. *Analytical Chemistry* 1998; **70**:1870–1881.
- Hu L, Harrison DJ, Masliyah JH. Numerical model of electrokinetic flow for capillary electrophoresis. *Journal of Colloid and Interface Science* 1999; **215**:300–312.
- Mitchell M, Qiao R, Aluru NR. Meshless analysis of steady-state electro-osmotic transport. *Journal of Microelectromechanical Systems* 2000; **9**:435–449.
- Wood WL. *Practical Time-Stepping Schemes*. Oxford University Press: Oxford, 1990.
- Hung ES, Senturia SD. Generating efficient dynamical models for microelectromechanical systems from a few finite-element simulation runs. *Journal of Microelectromechanical Systems* 1999; **8**(3):280–289.
- Bangia AK, Batcho PF, Kevrekidis IG, Karniadakis GE. Unsteady two-dimensional flows in complex geometries: comparative bifurcation studies with global eigenfunctions expansions. *SIAM Journal on Scientific Computing* 1997; **18**(3):775–805.
- Gabbay LD, Mehner JE, Senturia SD. Computer-aided generation of nonlinear reduced-order dynamic macromodels—i: no-stress-stiffened case. *Journal of Microelectromechanical Systems* 2000; **9**(2):262–269.
- Lall S, Marsden JE, Glavaski S. Empirical model reduction of controlled nonlinear systems. *Technical report CIT-CDS-98-008*, 1998.
- Berkooz G, Holmes P, Lumley JL. The proper orthogonal decomposition in the analysis of turbulent flows. *Annual Reviews of Fluid Mechanics* 1993; **25**:539–575.
- Cheng HS, Pan CHT. Stability analysis of gas-lubricated, self-acting, plain, cylindrical, journal bearing of finite length, using Galerkin's method. *Journal of Basic Engineering* 1965; **87**:185–192.
- Loeve M. *Probability Theory*. Van Nostrand: Princeton, N.J., 1963.
- Soderman O, Jonsson B. Electro-osmosis: Velocity profiles in different geometries with both temporal and spatial resolution. *Journal of Chemical Physics* 1996; **105**:10300–10311.
- Fan ZH, Harrison DJ. Micromachining of capillary electrophoresis injectors and separators on glass chips and evaluation of flow at capillary intersection. *Analytical Chemistry* 1994; **66**:177–184.
- Aluru NR, Li G. Finite cloud method: A true meshless technique based on a fixed reproducing kernel approximation. *International Journal for Numerical Methods in Engineering* 2001; **50**(10):2373–2410.
- Lumley JH. *Transition and Turbulence*. Academic Press: New York, 1981.
- Park HM, Lee MW. An efficient method of solving the Navier–Stokes equations for flow control. *International Journal for Numerical Methods in Engineering* 1998; **41**:1133–1151.
- Park HM, Lee MW. Control of Navier–Stokes equations by means of mode reduction. *International Journal for Numerical Methods in Engineering* 2000; **33**:535–557.
- Shvartsman SY, Kevrekidis IG. Nonlinear model reduction for control of distributed systems: a computer-assisted study. *AIChE Journal* 1998; **44**(7):1579–1595.
- Graham MD, Kevrekidis IG. Alternative approaches to the Karhunen–Loève decomposition for model reduction and data analysis. *Computers and Chemical Engineering* 1996; **20**(5):495–506.
- Park HM, Cho DH. The use of the Karhunen–Loève decomposition for the modelling of distributed parameter systems. *Chemical Engineering Science* 1996; **51**(1):81–98.
- Qiao R, Aluru NR. Mixed-domain and reduced-order modelling of electro-osmotic transport in bio-mems. *Technical Proceedings of the 2000 IEEE/ACM International Workshop on Behaviour Modelling and Simulation* Orlando, FL, USA, October 2000; 51–56.
- Rempfer D. On low-dimensional Galerkin models for fluid flow. *Theoretical and Computational Fluid Dynamics* 2000; **14**:75–88.
- Li G, Aluru NR. Boundary cloud method: a combined scattered point/boundary integral approach for boundary-only analysis. *Computer Methods in Applied Mechanics and Engineering* 2002; **191**:2337–2370.
- Mitchell MJ. Meshless analysis of electro-osmotic transport in μ Tas. *Master's Thesis*, University of Illinois at Urbana-Champaign, May 2000.